

Modelling the Nonlinear Shear Stress–Strain Behavior of a Carbon Fabric Reinforced Polyphenylene Sulphide From Rail Shear and $[(45^\circ, -45^\circ)]_{4s}$ Tensile Test

Ives De Baere, Wim Van Paepegem, Joris Degrieck

Department of Mechanical Construction and Production, Faculty of Engineering,
Ghent University, Sint-Pietersnieuwstraat 41, B-9000 Gent, Belgium

In this article, the nonlinear shear stress–strain relationship of a carbon fabric-reinforced polyphenylene sulphide is investigated by performing and comparing both the $[(+45^\circ/-45^\circ)]_{ns}$ tensile test and the three-rail shear test. First, quasi-static and hysteresis tests are performed to obtain the data necessary for the material model. Then, the material constants are optimized by comparing finite element simulations with the data derived from the experiments. The conducted experiments are simulated and the results are compared with the experiments, with excellent correspondence. POLYM. COMPOS., 30:1016–1026, 2009. © 2008 Society of Plastics Engineers

INTRODUCTION

There are several ways of inducing a state of in-plane shear [1, 2] in a composite to model the shear stress–strain relationship. Examples are the Iosipescu test [1, 3–5], the 10° off-axis test [4–7], the $[(+45^\circ/-45^\circ)]_{ns}$ tensile test [6, 8, 9, 10–12], the two- and three-rail shear test [13–16], torsion of a rod [17] and torsion of thin-walled tubes [18–21].

In this article, the nonlinear shear stress–strain behavior is studied by performing and comparing the $[(+45^\circ/-45^\circ)]_{ns}$ tensile test, as described in the *ASTM D3519/D3518M-94 (2001) standard test method for in-plane shear response of polymer matrix composite materials by tensile test of a $\pm 45^\circ$ laminate* and the three-rail shear test, as described in the *ASTM D 4255/D 4255M The standard test method for in-plane shear properties of polymer matrix composite materials by the rail shear method*. For the latter, however, a modified design of the three-rail shear test, as proposed by the authors in Ref. 22 is used.

The authors have already modelled the nonlinear shear stress–strain behavior of a glass fibre-reinforced epoxy, by

performing $[(+45^\circ/-45^\circ)]_{ns}$ tensile tests and 10° off-axis tests [6, 23]. The material for which the behavior is modelled in this study, is a carbon fabric reinforced polyphenylene sulphide (PPS), which is of a totally different nature than the one used in the previous study [6, 23]: (i) carbon fabric *versus* unidirectional glass fibre reinforcement and (ii) thermoplastic matrix *versus* thermosetting epoxy.

However, rather than developing an entirely new model, the same model as given in Ref. 23 is used to prove that the approach used by the authors in Refs. 6, 23 may be considered applicable to a wide range of materials.

In the next section, the used material and equipment are presented in more detail. Next, a paragraph concerning the conducted experiments is given and data for the material model are extracted. This is followed by the finite element modelling of both experiments and finally, conclusions are drawn.

MATERIALS AND METHODS

Composite Material

The material under study was a carbon fibre-reinforced polyphenylene sulphide (PPS), called CETEX. This material is supplied to us by TenCate, Almelo, NL. The fibre type is the carbon fibre T300J 3K and the weaving pattern is a 5-harness satin weave fabric with a mass per surface unit of 286 g/m^2 . The 5-harness satin weave is a fabric with high strength in both directions and excellent bending properties.

The carbon PPS plates were hot pressed and two stacking sequences were used for this study, namely a $[(0^\circ, 90^\circ)]_{4s}$ where $(0^\circ, 90^\circ)$ represents one layer of fabric and a $[(45^\circ, -45^\circ)]_{4s}$ which is a $[(0^\circ, 90^\circ)]_{4s}$ cut under a 45° angle with respect to the fibre orientation.

The in-plane elastic properties of the individual carbon PPS lamina were determined by the dynamic modulus identification method as described in Ref. 24 and are listed in Table 1.

Correspondence to: Ives De Baere; e-mail: ives.debaere@ugent.be
Contract grant sponsor: University research fund BOF (Bijzonder Onderzoeksfonds UGent).
DOI 10.1002/pc.20650
Published online in Wiley InterScience (www.interscience.wiley.com).
© 2008 Society of Plastics Engineers

TABLE 1. In-plane elastic properties of the individual carbon/PPS lamina (dynamic modulus identification method).

E_{11}	56.0	GPa
E_{22}	57.0	GPa
ν_{12}	0.033	—
G_{12}	4.175	GPa

The tensile strength properties were determined at the Technical University of Delft and are listed in Table 2.

The test coupons were sawn with a water-cooled diamond tipped saw.

Equipment

All experiments were performed on a servo-hydraulic INSTRON 8801 tensile testing machine with a FastTrack 8800 digital controller and a load cell of ± 100 kN.

For the registration of the tensile data, a combination of a National Instruments DAQpad 6052E for fireWire, IEEE 1394, and the SCB-68 pin shielded connector were used. The load, displacement, and strain, given by the FastTrack controller, as well as the extra signals from strain gauges and thermocouple were sampled on the same time basis.

The Material Model

Before discussing the experiments, the used material model is commented on to clarify which parameters are important for the model.

As mentioned in the introduction, the same model as proposed by the authors in Ref. 23 will be used in this article, to illustrate the general nature of the model. The shear stress–strain relationship is given by

$$\tau_{12} = G_{12}^0 \cdot (1 - D_{12}) \cdot (\gamma_{12}^{\text{total}} - \gamma_{12}^{\text{elast}}) \quad (1)$$

$$D_{12} = 1 - \frac{G_{12}^*}{G_{12}^0}$$

where, τ_{12} is the shear stress; G_{12}^0 is the initial shear stiffness; G_{12}^* is the shear stiffness of the damaged material; D_{12} is the damage parameter, which indicates the stiffness degradation; $\gamma_{12}^{\text{total}}$ is the total shear strain, given by the sum of the elastic and the permanent shear strain; $\gamma_{12}^{\text{perm}}$ is the permanent shear strain.

TABLE 2. Tensile strength properties of the individual carbon/PPS lamina (Mechanical testing at TUDelft).

X_T	732.0	MPa
$\varepsilon_{11}^{\text{ult}}$	0.011	—
Y_T	754.0	MPa
$\varepsilon_{22}^{\text{ult}}$	0.013	—
S_T	110.0	MPa

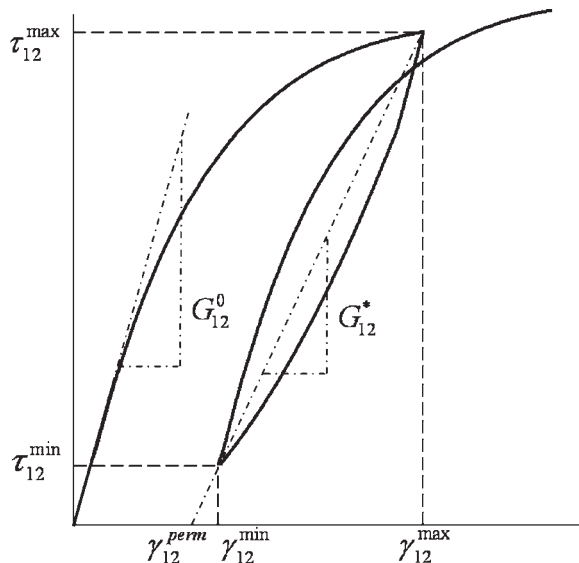


FIG. 1. Definition of the shear modulus G_{12}^* and the permanent shear strain $\gamma_{12}^{\text{perm}}$.

Figure 1 shows how the values of G_{12}^* and $\gamma_{12}^{\text{perm}}$ can be derived from the experimental data.

EXPERIMENTS AND DISCUSSION

$[(45^\circ, -45^\circ)]_{4s}$ Experiments

These tests were done according the ASTM D3519/D3518M-94 (2001) standard test method for in-plane shear response of polymer matrix composite materials by tensile test of a $\pm 45^\circ$ laminate. The dimensions of the used coupons are shown in Fig. 2.

All tensile tests were done in a displacement-controlled manner with a displacement speed of 2 mm/min, during which the force F , the longitudinal and transverse strains ε_{xx} and ε_{yy} , and the temperature was recorded. With these values, the shear stress τ_{12} and shear strain γ_{12} can be calculated as

$$\tau_{12} = \frac{1}{2} \frac{F}{w \cdot t} \quad (2)$$

$$\gamma_{12} = \varepsilon_{xx} - \varepsilon_{yy}$$

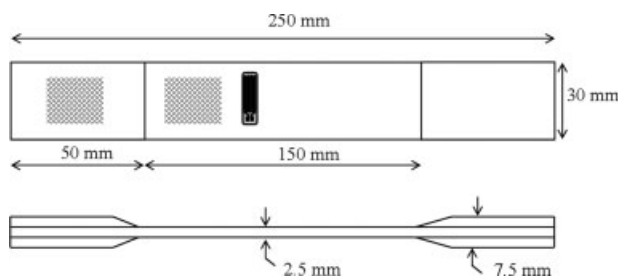


FIG. 2. Dimensions of the used $[(45^\circ, -45^\circ)]_{4s}$ tensile coupon, equipped with chamfered tabs of $[(45^\circ, -45^\circ)]_{4s}$ carbon PPS.

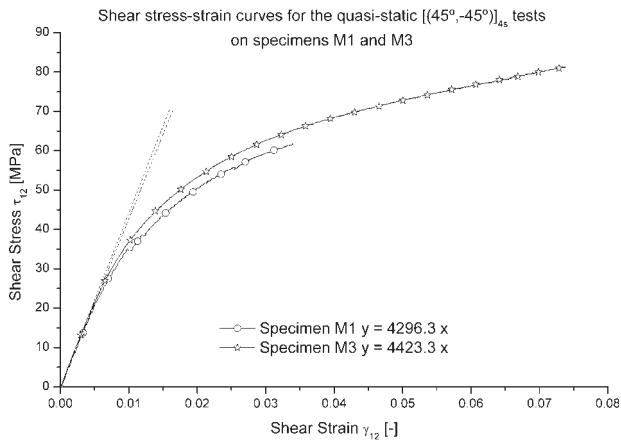


FIG. 3. Evolution of the shear stress as a function of the shear strain for the quasi-static tensile experiments.

where τ_{12} is the shear stress; F is the tensile force; w is the width of the specimen; t is the thickness of the specimen; γ_{12} is the total shear strain; ϵ_{xx} is the longitudinal strain; ϵ_{yy} is the transverse strain.

The transverse strain was measured using a strain gauge and the longitudinal strain was measured using the extensometer.

Figure 3 illustrates the highly nonlinear shear stress-strain evolution for two quasi-static experiments, M1 and M3. The curve is only depicted until the transverse strain gauge either saturated which was the case for M3, or debonded which happened for M1. The failure stresses were 105.4 and 105.3 MPa for M1 and M3 respectively. These values show good correspondence with the value given in Table 2. The stiffness could also be calculated from these results, as is shown in Fig. 3. Although some scatter is present on these values, they still correspond quite well with the values given in Table 1. During these tests, no increase in temperature was recorded.

Next, the hysteresis experiments were performed to obtain the data, necessary for the material model. The specimens were loaded until a maximum shear stress of 20 MPa was reached and then completely unloaded. For each of the next cycles, the maximum shear stress was increased with 10 MPa with respect to the previous cycle. This was repeated until the strain gauge failed or debonded. The value of 20 MPa was chosen because only very limited nonlinear behavior is visible in Fig. 3 before this value is reached.

Figure 4 illustrates the shear stress-strain evolution for three specimens M2, M4 and M5. For M4, the cycle after 60 MPa was reversed just before the strain gauge was expected to saturate. For M2 and M5, the strain gauge debonded after the cycle of 60 MPa. Failure stresses were 109.8 MPa for M2, 116.3 MPa for M4 and 103.8 MPa for M5. Again these values correspond very well with the value given in Table 2. The initial stiffness is also calculated and is shown in Fig. 4. Again, there is some scatter on the results, but the values correspond quite well with

those found in Fig. 3 and with the value determined by the dynamic modulus identification method (Table 1). It should be noted that the reproducibility of M2 and M4 is very high. Specimen M5 tends to behave stiffer during the entire specimen, without any apparent reason.

During these experiments, a very slight increase in temperature was noted of about 1°C.

Finally, Fig. 5 illustrates the occurring fracture for specimen M2, but this type of failure was seen for all the $[(45^\circ, -45^\circ)]_{45}$ tensile tests. The local narrowing before final failure can clearly be distinguished.

Using the same method as presented by the authors in Ref. 6 and illustrated in The Material Model, the following evolutions for permanent deformation (see Fig. 6) and stiffness degradation (see Fig. 7) are found.

The results are very reproducible for both damage parameters. It should be noted that there is a significant scatter on the damage parameter D_{12} for low total shear strains. This is due to the fact that the strains are very low and therefore, the determination of the slope of the hysteresis loop, as described in Ref. 6, is a lot more sensitive to noise and scatter on the strain measurement.

These data will be used for determining the material constants in Implementing the Material Model.

Three-Rail Shear Tests

These tests were done according to the ASTM D4255/D4255M “standard test method for in-plane shear properties of polymer matrix composite materials by the rail shear method” but the modified three-rail shear design, as documented in Ref. 22 is used. This design is illustrated in Fig. 8 and differs from the standard setup since the new design no longer requires bolts mounted through the specimen. The gripping is based on friction and geometrical clamping and the bolts are used to press a load transfer plate against the specimen, generating the normal force, necessary for the frictional clamping.

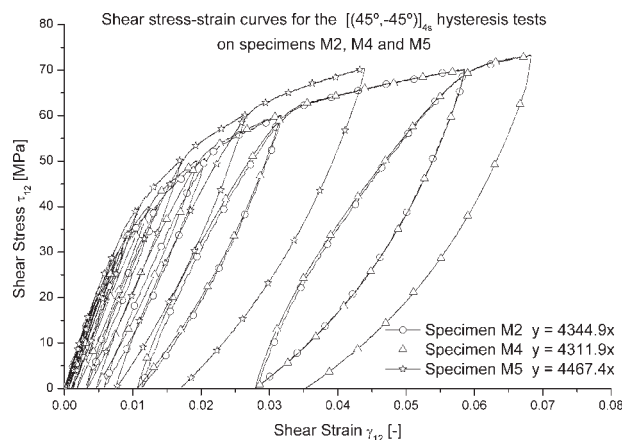


FIG. 4. Evolution of the shear stress as a function of the shear strain for the tensile hysteresis experiments.

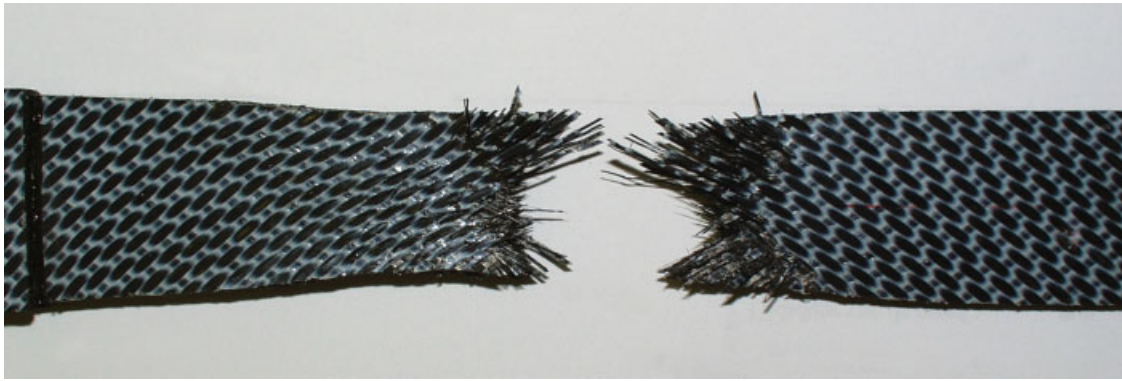


FIG. 5. Image of the fracture of a $[(45^\circ, -45^\circ)]_{4s}$ specimen. [Color figure can be viewed in the online issue, which is available at www.interscience.wiley.com.]

The dimensions of the used specimen are given in Fig. 9.

All tests were done in a displacement-controlled manner with a displacement speed of 1 mm/min, during which the force F , the strains ε_i , $i = 1,2,3,4$ and the temperature were recorded. With these values, the shear stress and strain can be calculated as

$$\begin{aligned} \tau_{12} &= \frac{1}{2} \frac{F}{t \cdot h} \\ \gamma_{12} &= |\varepsilon_i - \varepsilon_j| \end{aligned} \quad (3)$$

where h is the height of the specimen and t the thickness; (i,j) is either (1,2) or (3,4) with respect to the numbering of the strain gauges in Fig. 9. A few results from quasi-static tests are given in Fig. 10. Since from each rail shear test, two curves can be derived, one from each instrumented loaded zone, there should be six curves for three specimens. However, in Fig. 10, only the curves from the strain gauges which lasted the longest are given; the tests were stopped once all strain gauges de-bonded or saturated which means that the maximum value of the shear stress and strain in Fig. 10 do not correspond with failure.

After saturation or failure, the test was stopped, so the possibility for non-destructive evaluation of the specimens remained an option.

It should be noticed that the results from these quasi-static tests are very reproducible and that the calculated stiffness corresponds very well with the value obtained with the dynamic modulus identification method (Table 1). Furthermore, the shear stress–strain evolution also corresponds very well with the one from the $[(45^\circ, -45^\circ)]_{4s}$ tensile test (see Fig. 3). During the quasi-static rail shear tests, no temperature increase was measured.

Next, hysteresis tests were performed, using the same principle as for the $[(45^\circ, -45^\circ)]_{4s}$ tensile test, but starting with a maximum shear stress of 10 MPa and increasing 10 MPa with each loading. The lower starting value of 10 MPa was chosen to verify that little damage occurs for these low load levels. The results from these are given in Fig. 11 and again, only the curves from the strain gauges which lasted the longest, are plotted. The omitted curves, however, showed very good correspondence with the corresponding depicted ones. Again it should be noted the results are very much alike and that the initial stiffness corresponds very well with the value given in Table 1.

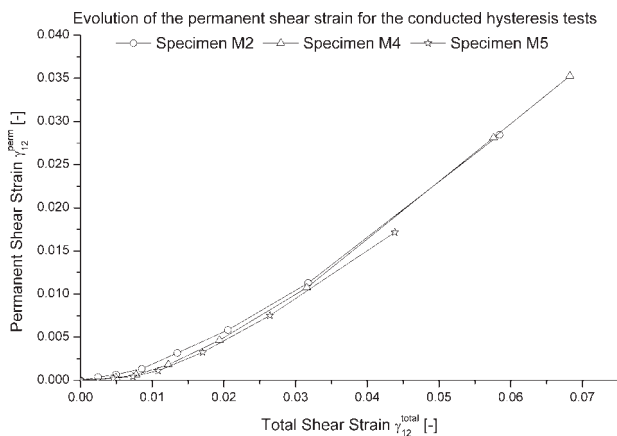


FIG. 6. Evolution of the permanent shear strain during the hysteresis experiment.

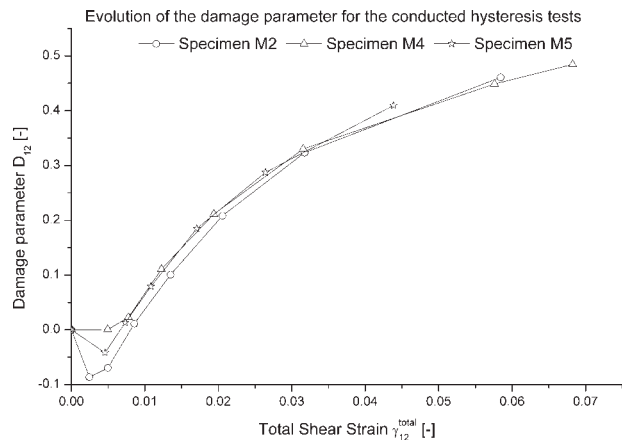


FIG. 7. Evolution of the damage parameter during the hysteresis experiment.



FIG. 8. The modified three-rail shear setup, as presented in [22]. [Color figure can be viewed in the online issue, which is available at www.interscience.wiley.com.]

During the hysteresis tests, an increase of about 1°C was measured.

Again, using the same method as illustrated in The Material Model to determine permanent deformation and stiffness degradation from a cyclic shear stress–strain curve, the following evolutions are found for $\gamma_{12}^{\text{perm}}$ (see Fig. 12) and D_{12} (see Fig. 13). It should be noticed that these evolutions show very good correspondence with the damage parameters obtained from the $[(45^{\circ}, -45^{\circ})]_{4s}$ tensile tests.

Again, there is some scatter on the damage parameter D_{12} for low values of the total shear strain, but as men-

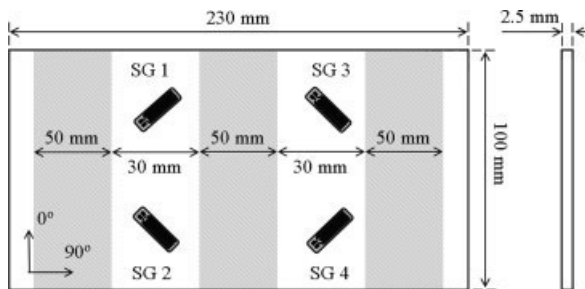


FIG. 9. Dimensions of the used $[(0^{\circ}, 90^{\circ})]_{4s}$ three-rail shear specimen. The location of the strain gauges, as well as the clamps, is also illustrated.

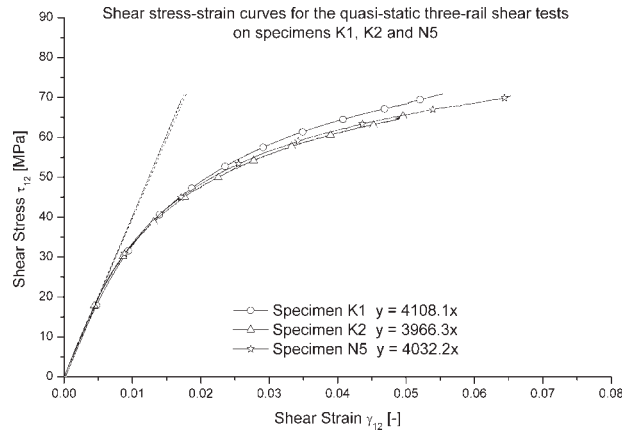


FIG. 10. Evolution of the shear stress as a function of the shear strain for the quasi-static three-rail shear experiments.

tioned before, this is due to the fact that the strains are very low and therefore, the determination of the slope of the hysteresis loop, as described in Ref. 6 is more sensitive to scatter and noise on the measured strains.

These data will also be used for determining the material constants in the following section.

FINITE ELEMENT MODELLING

Implementing the Material Model

For this model, the evolution of D_{12} and $\gamma_{12}^{\text{perm}}$ are given by the following equations:

$$\frac{d\gamma_{12}^{\text{perm}}}{d\gamma_{12}^{\text{total}}} = C_1 \cdot |\gamma_{12}^{\text{total}}| \cdot \exp(C_2 \cdot |\gamma_{12}^{\text{perm}}|) \quad (4)$$

$$\frac{dD_{12}}{d\gamma_{12}^{\text{elast}}} = C_3 \cdot \exp(C_4 \cdot D_{12})$$

where $\gamma_{12}^{\text{perm}}$ is the permanent shear strain; $\gamma_{12}^{\text{total}}$ is the total shear strain, given by the sum of the elastic and the per-

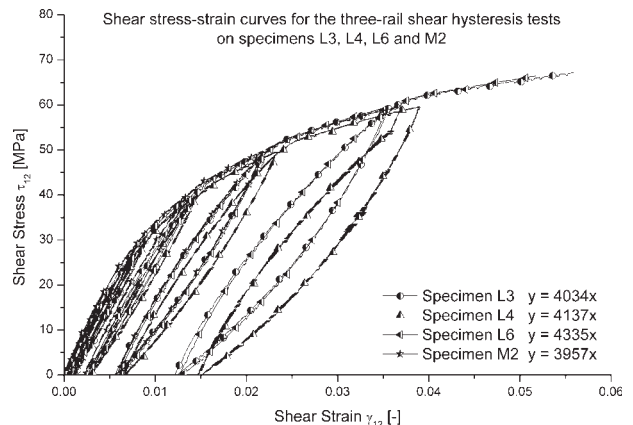


FIG. 11. Evolution of the shear stress as a function of the shear strain for the rail shear hysteresis experiments.

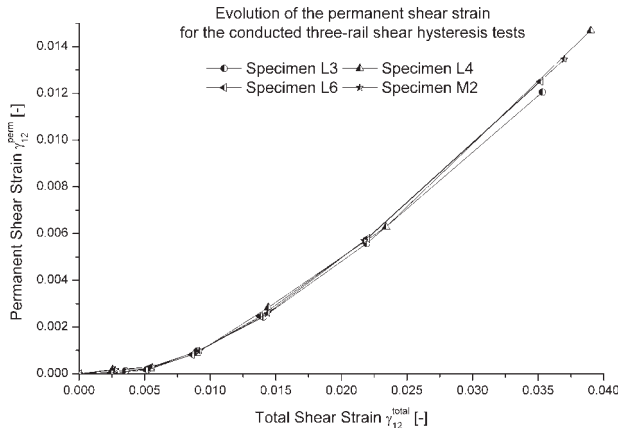


FIG. 12. Evolution of the permanent shear strain during the three-rail shear hysteresis experiment.

manent shear strain; D_{12} is the damage parameter, which indicates the stiffness degradation; γ_{12}^{elast} is the elastic shear strain; C_1, C_4 are the material constants.

For the finite element modelling, ABAQUS Standard was used. The latter is capable of working with user-defined material models, using a subroutine called UMAT. To implement the material model in UMAT, it must first be written using finite differences. This yields for Eq. 4, with $\gamma_{12}^{elast} = \gamma_{12}^{total} - \gamma_{12}^{perm}$:

$$\begin{aligned} \gamma_{12}^{perm,new} &= \gamma_{12}^{perm,old} + C_1 \cdot |\gamma_{12}^{total,new}| \cdot \exp(C_2 \cdot |\gamma_{12}^{perm,old}|) \\ &\quad \cdot (\gamma_{12}^{total,new} - \gamma_{12}^{total,old}) \\ D_{12}^{new} &= D_{12}^{old} + C_3 \cdot \exp(C_4 \cdot D_{12}^{old}) \cdot [(|\gamma_{12}^{total,new}| - |\gamma_{12}^{perm,new}|) \\ &\quad - (|\gamma_{12}^{total,old}| - |\gamma_{12}^{perm,old}|)] \end{aligned} \quad (5)$$

In this equation, the superscript “old” refers to the values obtained from the previous time step and the superscript “new” refers to the value necessary for the current time step.

Next, Eq. 1 can be implemented. However, after some test runs with UMAT, it became clear that a converging solution could only be found if stresses are calculated

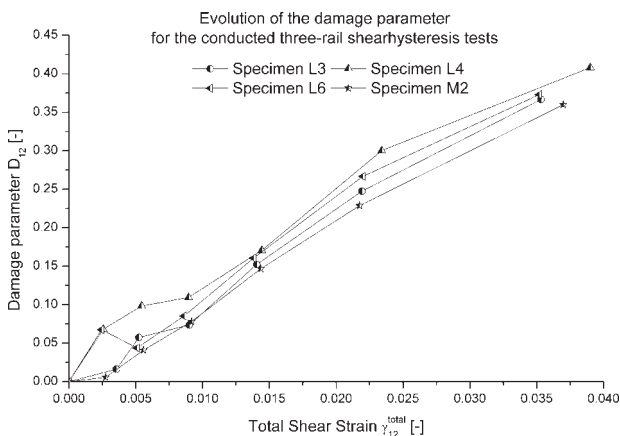


FIG. 13. Evolution of the damage parameter during the three-rail shear hysteresis experiment.

with stress increments, meaning the strain increments must be used, rather than calculating the stress using the total strains. As such, Eq. 1 must be rewritten with finite differences. This yields:

$$\begin{aligned} \tau_{12}^{new} &= G_{12}^0 \cdot (1 - D_{12}^{new}) \cdot (\gamma_{12}^{total,new} - \gamma_{12}^{perm,new}) \\ \tau_{12}^{old} &= G_{12}^0 \cdot (1 - D_{12}^{old}) \cdot (\gamma_{12}^{total,old} - \gamma_{12}^{perm,old}) \end{aligned} \quad (6)$$

Hence, the following equation is derived for the stress:

$$\begin{aligned} \tau_{12}^{new} &= \tau_{12}^{old} + G_{12}^0 \cdot (1 - D_{12}^{new}) \cdot [(\gamma_{12}^{total,new} - \gamma_{12}^{total,old}) \\ &\quad - (\gamma_{12}^{perm,new} - \gamma_{12}^{perm,old})] - G_{12}^0 \cdot (D_{12}^{new} - D_{12}^{old}) \\ &\quad \cdot (\gamma_{12}^{total,old} - \gamma_{12}^{perm,old}) \end{aligned} \quad (7)$$

The sum in Eq. 7 consists of two terms: the first is the expected one, giving a stress increment using the increment in elastic strain. The second term is the result of the use of stress increments and must not be forgotten.

Next, the modelling in ABAQUS of the two test geometries is discussed.

The $[(45^\circ, -45^\circ)]_{4s}$ Test

For these simulations, only the loaded part of the specimen was modelled, resulting in a rectangular specimen of 150 mm by 30 mm. Symmetry was not used because this would yield images of stress distributions which are a little more difficult to interpret than if the entire specimen is modelled. Figure 14 depicts the used mesh and boundary conditions.

The specimen was meshed using a 3D quadratic brick element with reduced integration; the size of the mesh was 4 mm and eight elements through the thickness were used. An extra simulation was performed with a mesh size of 2 mm, to assess whether the mesh size has significant influence on the model. The following boundary conditions were applied:

- Plane A, the left side of the loaded zone, was fixed along the 1- and 2-axis, simulating the rigid grip.
- Plane B, the right side of the loaded zone, was fixed along the 1- axis and given a displacement of 10 mm along the 2-axis. This value corresponds with the value at which point the strain gauges in the experiments debonded or saturated.
- Plane C, the central plane of the loaded zone, was fixed along the 3-axis

Since it is a 3D analysis, there are no rotational degrees of freedom. Because of the large deformations, a geometrically nonlinear simulation was performed.

The Three-Rail Shear Test

For these simulations, only the loaded part of the specimen was modelled and because of symmetry, only half of the specimen was drawn, Fig. 15 depicts the used mesh and boundary conditions.

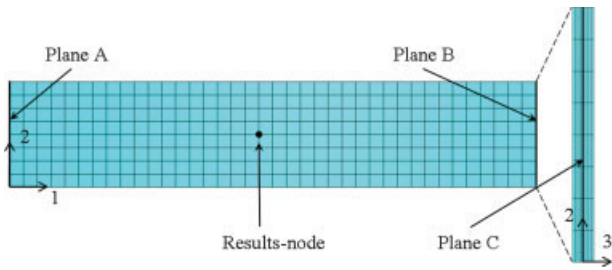


FIG. 14. Used mesh for the finite element simulations of the $[(45^\circ, -45^\circ)]_{4s}$ tensile test. [Color figure can be viewed in the online issue, which is available at www.interscience.wiley.com.]

The specimen was meshed using a 3D quadratic brick element with reduced integration; the size of the mesh was 3 mm and eight elements through the thickness were used. An extra simulation was performed with a mesh size of 1 mm, also to assess the influence of the mesh size on the output of the material model. The width of the modelled specimen was 30 mm and the height 100 mm, as was the case in the experiments. The following boundary conditions were applied:

- Plane A, the right side of the loaded zone, was fixed along the 1- and 2-axis.
- Plane B, the left side of the loaded zone, was fixed along the 1- axis and given a displacement of 3 mm along the 2-axis. This value corresponds with the value at which point the strain gauges in the experiments debonded or saturated.
- Plane C, the central plane of the loaded zone, was fixed along the 3-axis.

Since it is a 3D analysis, there are no rotational degrees of freedom. Because of the large deformations, a geometrically nonlinear simulation was performed.

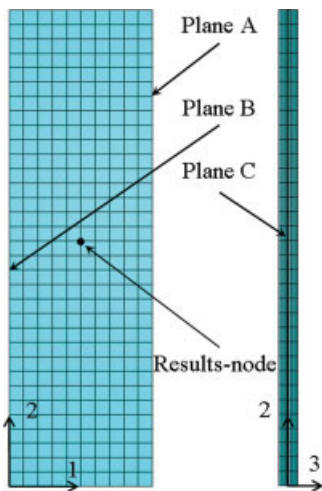


FIG. 15. Used mesh for the finite element simulations of the three-rail shear test. [Color figure can be viewed in the online issue, which is available at www.interscience.wiley.com.]

Discussion of the Simulations

Of course, first the material constants C_1 till C_4 need to be determined. These values have been determined by the combined optimisation of the evolutions of shear stress, shear strain, γ_{12}^{perm} , and D_{12} on the experimental results, given in Figs. 3, 6, 7, 10, 12, and 13, respectively.

This optimisation has been done using a nonlinear least square solver. With a starting set of material constants, a finite element simulation is conducted and afterwards, the evolutions of shear stress, shear strain, γ_{12}^{perm} , and D_{12} are derived. Then, the solver compares these values with the experimental ones and suggests a new set of material constants, which are then used as starting values for the next iteration. This is repeated until a minimum value of the sum of the squared differences between numerical and experimental values is achieved.

This yielded the following combination of material constants:

$$C_1 = 29 \quad C_2 = -35 \quad C_3 = 16 \quad C_4 = -0.1 \quad (8)$$

For both the three-rail shear and the $[(45^\circ, -45^\circ)]_{4s}$ tensile test simulation, the evolution of the shear stress, shear strain, permanent shear strain γ_{12}^{perm} , and damage parameter D_{12} was plotted for a node in the centre of the specimen (Results-node in Figs. 14 and 15), so that the stress concentrations near the clamps did not have any influence. These results are given in Figs. 16, 17, and 18 respectively.

It should be remarked that there is an excellent correspondence for all three evolutions and that refining the mesh, for both the three-rail shear as the $[(45^\circ, -45^\circ)]_{4s}$ simulations does not have a significant effect.

In the shear stress–strain evolution, depicted in Fig. 16, it can be seen that after a certain strain level is reached, the total strain tends to decrease, as well as the corresponding shear stress. The corresponding damage and permanent shear strain remain constant during this decrease.

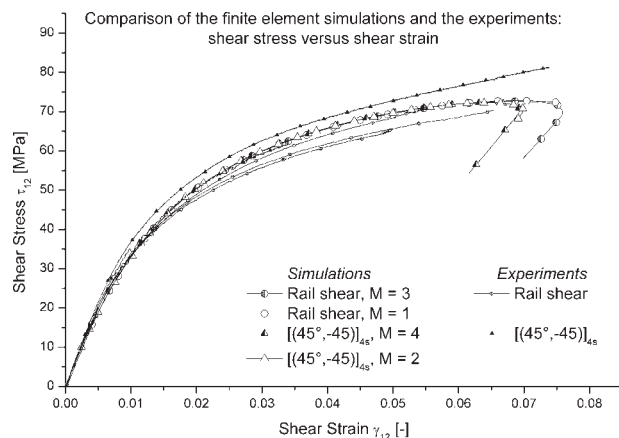


FIG. 16. Evolution of the shear stress as a function of the shear strain for both the simulations and the experiments.

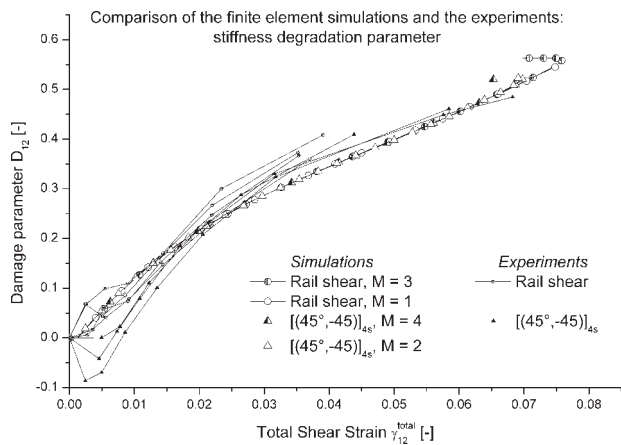


FIG. 17. Evolution of the permanent shear strain for both the simulations and the experiments.

This happens for both types of experiments and is the result of a stress relief in the centre of the specimen, due to localization of the total shear strain elsewhere in the specimen. This can be easily shown in the $[(45^\circ, -45^\circ)]_{4s}$ simulations. Fig. 19 depicts the total shear strain at three well chosen time-steps. Time-step 45 represents the end of the increase in shear strain, Time step 58 is the last time-step available and time-step 51 is chosen for an intermediate distribution plot. The deformation is scaled by 1.5 to visualize the reason more clearly.

From these different stages in time, it can clearly be seen that the fast narrowing of the specimen near the clamped ends results in a high increase in shear strain (the dark X on the contour plots). Since the simulation is done displacement controlled, corresponding with the experiment, the shear strain in the centre of the specimen is allowed to relax. Given the fact that the permanent shear strain is not allowed to decrease, this renders a decrease in elastic shear strain and as a result, a decrease in shear stress. Fig. 20 shows this localization in three stages as it could be seen in the experiment.

This decrease in shear stress and strain was not seen in the experiments, but the localization of the total shear strain occurred after the strain gauge saturated and the strain measurement was stopped.

Finally, in Figs. 21 and 22, the distributions of the shear stress and the damage model parameters are given for the time step at which maximum stress in the central area is reached. The shear stress distribution is very uniform, with exception near the clamped ends, where a cross-like shape can be distinguished. However, this uniform distribution is still the main reason why the $[(45^\circ, -45^\circ)]_{4s}$ is chosen to characterize the shear behavior of a composite. The permanent shear strain is also relatively uniform, although higher values are reached where the specimen is most likely to narrow. The damage parameter D_{12} also indicates where failure is most likely to occur.

For the three-rail shear test, also a very uniform shear stress distribution can be seen. The distribution of both damage and permanent deformation clearly indicate where failure will start, namely in the vicinity of the clamps. This was also derived by Lessard et al. [16]. A possibility for future research could be to investigate whether the use of notches, as was done in Ref. 16 would have the same effects on a fabric-reinforced composite.

CONCLUSIONS

In this article, the nonlinear shear stress-strain relationship of a carbon fabric-reinforced polyphenylene sulphide was investigated. The stress-strain data were obtained by performing both the $[(45^\circ, -45^\circ)]_{4s}$ tensile test, as described in the ASTM D3519/D3518M-94 (2001) standard test method for in-plane shear response of polymer matrix composite materials by tensile test of a $\pm 45^\circ$ laminate and the three-rail shear test, as described in the ASTM D 4 5/D 4255M The standard test method for in-plane shear properties of polymer matrix composite materials by the rail shear method. Both types of experiments yielded very similar results.

Then, the behavior was modelled using a previously derived material model, which has two damage parameters: (i) D_{12} which represents the shear stiffness degradation and (ii) the permanent shear strain γ_{12}^{perm} , which represents the permanent shear deformation. This material model was then implemented in the finite element software ABAQUS/standard and both test setups were modelled. The four material constants of the material model were optimized based on the experimentally derived evolutions of shear stress-strain, D_{12} and γ_{12}^{perm} . Afterwards, the results from the simulations were compared with the experimental curves and a very good agreement was achieved.

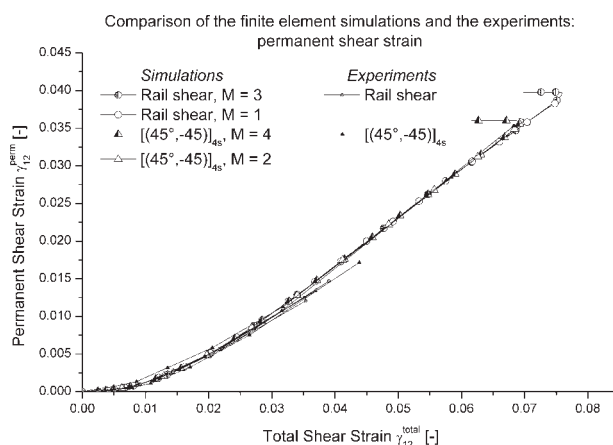


FIG. 18. Evolution of the damage parameter for both the simulations and the experiments.

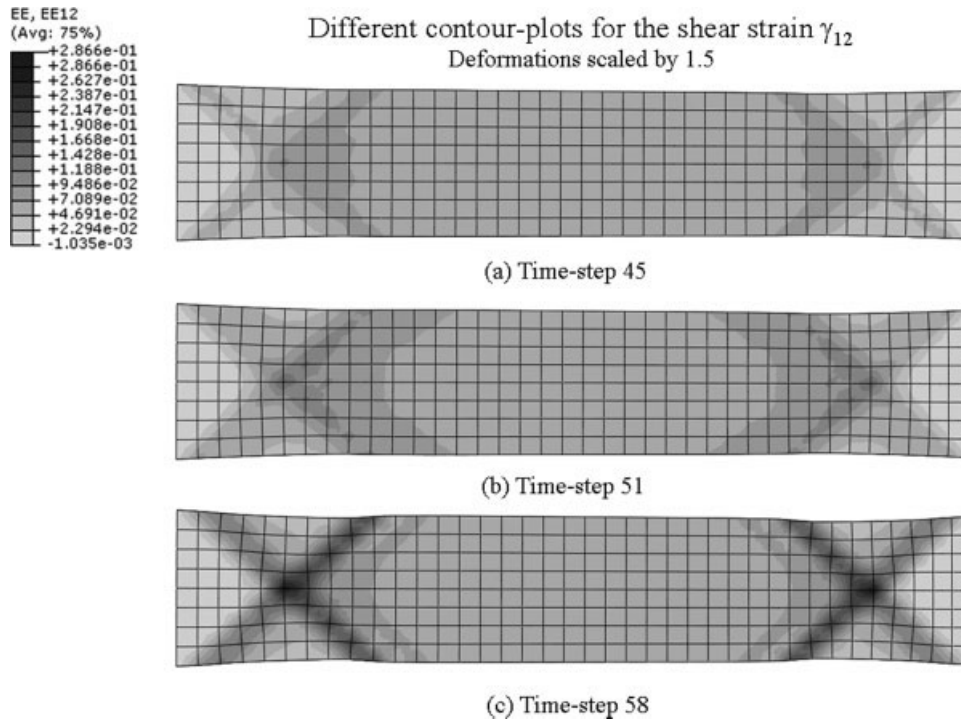


FIG. 19. Illustration of the decrease in the shear strain in the centre of the specimen.

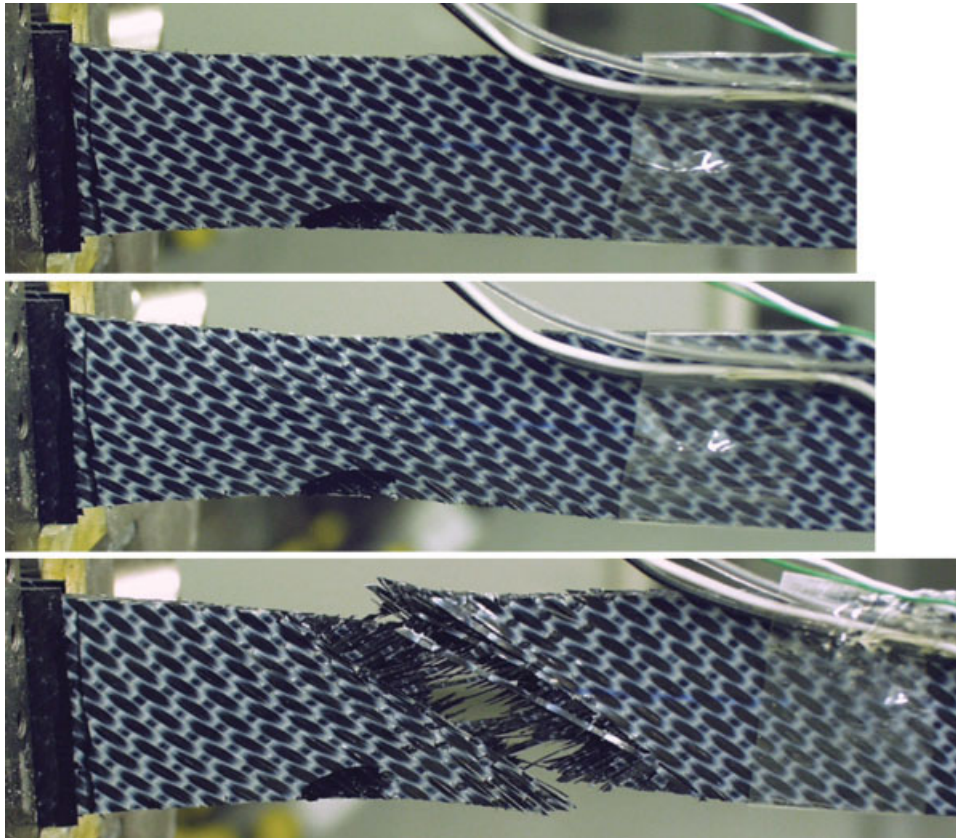


FIG. 20. Illustration of the experimental localization of the total shear strain. [Color figure can be viewed in the online issue, which is available at www.interscience.wiley.com.]

Different contour-plots for the $[(45^\circ, -45^\circ)]_{4s}$ tensile test
Deformations scaled by 1.5

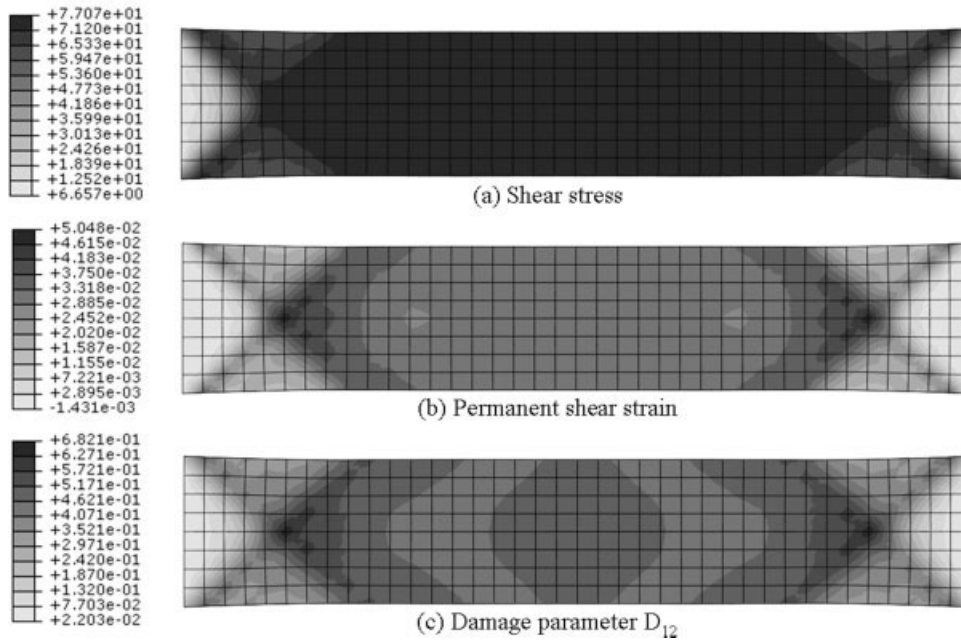


FIG. 21. Distribution of the (a) shear stress, (b) permanent shear strain and (c) damage parameter D_{12} for the $[(45^\circ, -45^\circ)]_{4s}$ simulation.

Different contour-plots for the three-rail shear
Deformations scaled by 1.5

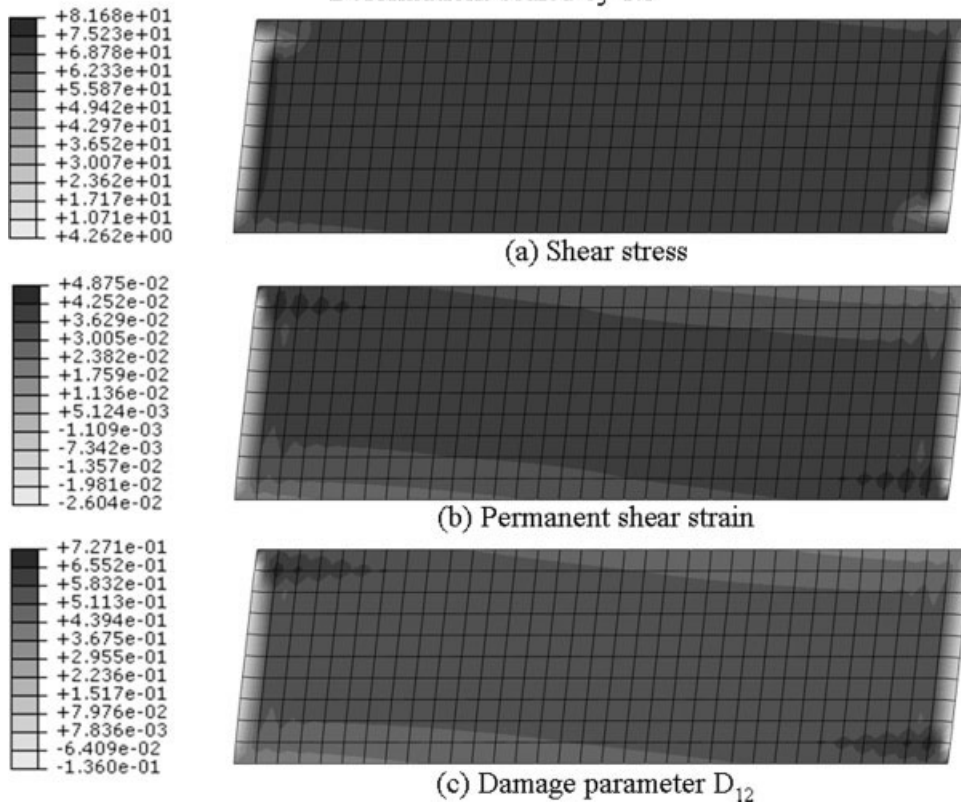


FIG. 22. Distribution of the (a) shear stress, (b) permanent shear strain and (c) damage parameter D_{12} for the three-rail shear simulation.

ACKNOWLEDGMENTS

The authors are highly indebted to the to Ten Cate Advanced Composites for supplying the material.

REFERENCES

1. Y.M. Tarnopol'skii, A.K. Arnautov, and V.L. Kulakov, *Compos. A: Appl. Sci. Manuf.*, **30(7)**, 879 (1999).
2. J.M. Whitney, I.M. Daniel, and R.B. Pipes, "Experimental Mechanics of Fiber Reinforced Composite Materials," *Composite Characterization, The Society for Experimental Mechanics*, Connecticut, 160 (1984), Chapter 4.
3. E.M. Odom, D.M. Blackketter, and B.R. Suratno, *Exp. Mech.*, **34(1)**, 10 (1994).
4. G. Odegard and M. Kumosa, *Comp. Sci. Technol.*, **60**, 2917 (2000).
5. F. Pierron and A. Vautrin, *J. Comp. Mater.*, **31(9)**, 889 (1997).
6. W. Van Paepegem, I. De Baere, and J. Degrieck, *Comp. Sci. Technol.*, **66(10)**, 1455 (2006).
7. F. Pierron and A. Vautrin, *Comp. Sci. Technol.*, **56**, 483 (1996).
8. A.T. Echtermeyer, "Evaluation of the [± 45]s Inplane Shear Test Method for Composites Reinforced by Multiaxial Fabrics," in *ECCM-CTS 2: Composites Testing and Standardisation*, P.J. Hogg, K. Schulte, and H. Wittich, Eds., European Conference on Composites Testing and Standardisation, 13–15 September, 1994, Woodhead Publishing Limited, Hamburg, Germany, 305 (1994).
9. S. Shalom, H. Harel, and G. Marom, *Comp. Sci. Technol.*, **57(9–10)**, 1423 (1997).
10. J. Payan and C. Hochard, *Int. J. Fatigue*, **24(2–4)**, 299 (2002).
11. U.A. Khashaba, *Comp. Struct.*, **65(2)**, 167 (2004).
12. T. Maeda, V. Baburaj and T. Koga, *Opt. Eng.*, **36(7)**, 1942 (1997).
13. A.K. Hussain and D.F. Adams, *J. Comp. Technol. Res.*, **21(4)**, 215 (1999).
14. A.K. Hussain and D.F. Adams, *Exp. Mech.*, **44(4)**, 354 (2004).
15. A.K. Hussain and D.F. Adams, *Comp. Sci. Technol.*, **64(2)**, 221 (2004).
16. L.B. Lessard, O.P. Eilers, and M.M. Shokrieh, *J. Reinf. Plast. Comp.*, **14(9)**, 965 (1995).
17. L. Ferry, D. Perreux, D. Varchon, and N. Sicot, *Comp. Sci. Technol.*, **59(4)**, 575 (1999).
18. A.M. El-Assal and U.A. Khashaba, *Comp. Struct.*, **79(4)**, 599 (2007).
19. D. Qi and G. Cheng, *Polym. Comp.*, **28(1)**, 116 (2007).
20. H. Kawakami, T.J. Fujii, and Y. Morita, *J. Reinf. Plast. Comp.*, **15(2)**, 183 (1996).
21. T. Fujii and F. Lin, *J. Comp. Mater.*, **29(5)**, 573 (1995).
22. I. De Baere, W. Van Paepegem, and J. Degrieck, *Polym. Test.*, submitted.
23. W. Van Paepegem, I. De Baere, and J. Degrieck, *Comp. Sci. Technol.*, **66(10)**, 1465 (2006).
24. I. De Baere, W. Van Paepegem, J. Degrieck, H. Sol, D. Van Hemelrijck, and A. Petreli, *Compos. A*, **38(9)**, 2047.
25. I. De Baere, W. Van Paepegem, and J. Degrieck, *Polym. Comp.*, accepted.